JOURNAL OF BACTERIOLOGY, Apr. 1993, p. 1946–1955
0021-9193/93/071946-10$02.00/0

Vol. 175, No. 7

Transmission Electron Microscopy, Scanning Tunneling Microscopy, and Atomic Force Microscopy of the Cell Envelope Layers of the Archaeobacterium *Methanospirillum hungatei* GP1

G. SOUTHAM,[1] M. FIRTEL,[1] B. L. BLACKFORD,[2] M. H. JERICHO,[2] W. XU,[2] P. J. MULHERN,[2] AND T. J. BEVERIDGE[1]*

Department of Microbiology, College of Biological Science, University of Guelph, Guelph, Ontario N1G 2W1,[1] and Department of Physics, Dalhousie University, Halifax, Nova Scotia B3H 3J5,[2] Canada

Received 10 August 1992/Accepted 16 September 1992

***Methanospirillum hungatei* GP1 possesses paracrystalline cell envelope components including end plugs and a sheath formed from stacked hoops. Both negative-stain transmission electron microscopy (TEM) and scanning tunneling microscopy (STM) distinguished the 2.8-nm repeat on the outer surface of the sheath, while negative-stain TEM alone demonstrated this repeat around the outer circumference of individual hoops. Thin sections revealed a wave-like outer sheath surface, while STM showed the presence of deep grooves that precisely defined the hoop-to-hoop boundaries at the waveform nodes. Atomic force microscopy of sheath tubes containing entrapped end plugs emphasized the end plug structure, suggesting that the sheath was malleable enough to collapse over the end plugs and deform to mimic the shape of the underlying structure. High-resolution atomic force microscopy has revised the former idea of end plug structure so that we believe each plug consists of at least four discs, each of which is ~3.5 nm thick. Pt shadow TEM and STM both demonstrated the 14-nm hexagonal, particulate surface of an end plug, and STM showed the constituent particles to be lobed structures with numerous smaller projections, presumably corresponding to the molecular folding of the particle.**

All current techniques for ultrahigh resolution of biomolecular structure have inherent drawbacks. For example, not only does transmission electron microscopy (TEM) usually require heavy metal contrasting agents, it also produces high energy loads and high vacuums on the specimen. Only in exceptional cases, such as the purple membrane of *Halobacterium* spp. (18), have molecular folding data been obtained. The inception of scanning tunneling microscopy (STM) (7) and atomic force microscopy (AFM) (6) has certainly made the atomic resolution of hard, inanimate surfaces feasible, and there is a good possibility that this same resolution can be approached in biology. STM and AFM are currently being used on a number of biostructures and their constituent biopolymers, but they are still relatively new techniques in structural biology, and submolecular resolution must be interpreted with caution since biomaterials are loosely bonded and easily deformable. Specimens must be chosen with care, and close attention must be paid to the possibility of induced artifacts. It is best to take a multitechnique approach which combines high-resolution methodologies based on different principles; uniformity of high-resolution detail from each ensures accuracy of interpretation. Using this rationale, we have combined TEM, STM, and AFM to study paracrystalline surfaces possessed by the archaeobacterium *Methanospirillum hungatei*.

STM and AFM rely on the raster scanning of a fine-tip probe over a surface, with piezoelectric ceramics to control movement to within subnanometer distances, which forms a topographical three-dimensional image of the specimen. In STM, the vertical tip displacement during scanning is dependent on the tunneling current between the penultimate atom at the tip and the underlying semiconductive or conductive surface (41). In AFM, the interatomic repulsive forces between the tip and the surface act to suspend the probe as it is moved, and imaging is possible on conductive and nonconductive surfaces (40). Since specimens can be scanned under ambient conditions with low energies, these microscopes offer a (potentially) powerful means of examining functioning molecules with usual AFM operating conditions (12). Currently, the resolution of atomic structure is only routinely achieved with hard crystalline surfaces (1, 7) and organic adsorbates such as smectic liquid crystal monolayers (28, 33). Subnanometer resolution of cellular surfaces has been difficult to achieve because of masking of atomic structure through the use of heavy metal contrasting agents and problems associated with the stabilization of the specimen during STM and AFM imaging (3, 14, 25, 37, 39).

M. hungatei GP1 is a methanogenic archaeobacterium which possesses several unique paracrystalline envelope structures (42). Two of these structures, the sheath (5) and the end plug (4), are resilient macromolecular assemblies. This property helps in their purification for detailed structural analysis.

The purified cylindrical sheath is composed of stacks of hoops (34) which are of constant diameter (~0.45 μm) and contain obvious 2.8-nm repeats on their outer circumference (by negative-stain TEM). It is a hollow cylinder about 8 μm long possessing 2.8-nm particles arranged in p2 symmetry on its outer surface (a = 2.8 nm, b = 5.6 nm, and γ = 86°) (38). Intact sheath is a specimen for STM or AFM with a characteristic rectangular shape and a striated surface (mul-

* Corresponding author.

tiples of 2.8 nm) that is easily distinguished from the substrate surface (3, 9, 10).

The end plug is a multilaminar structure which contains two different types of disc-shape proteinaceous assemblies (4). Both of these individual plug layers possess 18-nm repeats with different p6 packing arrangements: a particulate layer consisting of large, roughly circular 14-nm subunits, and a holey layer consisting of roughly circular pores (ca. 15 nm [2, 26]) defined by trimeric subunits.

The established high resolution by TEM and selected area electron diffraction of these structures and their well-defined boundaries and periodic features make them useful biological surfaces for further topographical elucidation by STM and AFM (3, 9–11). In the present study, the structural information obtained from negative strains, thin sections, and Pt-shadowed material by TEM is compared and contrasted with the structural evidence supplied by STM and AFM imaging. We have used STM and AFM in conjunction with TEM to obtain a more exact characterization of the sheath and end plug of *M. hungatei* beyond the degree of either STM, AFM, or TEM alone.

MATERIALS AND METHODS

Bacterium and growth conditions. *M. hungatei GP1* (23) was grown in an SA medium as described by Patel et al. (22).

Purification of cell envelope components. The cell envelope of *M. hungatei* consists of several boundary layers which can be seen in Fig. 1 and which are united with one another by complex chemical interactions. The sheath of *M. hungatei* is an extremely resilient structure (5) which allows its purification through a succession of harsh treatments: 0.1 N NaOH at room temperature and 1% (wt/vol) sodium dodecyl sulfate (SDS) at 100°C (29). Hoops were produced by chemically splitting the intact sheath along the hoop boundaries with 2% (wt/vol) SDS and 5% (vol/vol) concentrated β-mercaptoethanol (β-ME) (29).

Since the sheath purification regimen destroyed the end plugs, they were isolated by spheroplasting and lysing cells with 15 mM dithiothreitol at pH 9.6 (35). The resulting crude sheath-end plug preparation was cleaned of contaminating membrane material by washing (three times) with 0.1% (wt/vol) SDS in dithiothreitol buffer and centrifugation (14,000 × *g*). The end plugs were excised from the sheath cylinder by a 1% (wt/vol) SDS treatment at room temperature, and the sheath was separated from them by centrifugation (14,000 × *g*). The end plugs remained in suspension.

Sample preparation for TEM. The preparation of *M. hungatei* for thin-section analysis and of its cell envelope components for negative staining and Pt shadowing have been described (3, 29).

Sample preparation for STM and AFM. Cell envelope preparations were diluted to between 1.0 and 0.1 mg/ml in deionized water (NANOpure, Barnstead). Small volumes (2 to 4 μl) of sample were then applied to either highly ordered pyrolytic graphite (HOPG) (STM and AFM) or mica (AFM) and allowed to dry. These samples were washed twice with deionized water and dried; they were then ready for AFM. For routine STM analysis, samples were coated with between 2.5 and 5.0 nm Pt or C.

Operating conditions for STM. For STM, we utilized the piezoelectric bimorph design of Blackford et al. (8). For constant-tunneling current-mode STM, the *z* piezo feedback voltage was monitored while the tip was scanned across the surface. The visual three-dimensional image was provided by using *x* and *y* + *z* voltages as the *x* and *y* axes on the graph. The tunneling current was typically 0.1 nA, and the tip bias was −1.0 V. Most STM imaging was done on C- or Pt-coated samples.

Operating conditions for AFM. The AFM is based on a modified version of the bimorph STM (21). Si_3N_4 cantilevers were V shaped, carried Si_3N_4 tips, and were commercially obtained. Cantilever deflection was sensed with a fiber optic-coupled interferometer. These levers had force constants of less than 0.1 N/m.

RESULTS

Description of intact envelope and the use of two substrates for STM and AFM. The spatial relationship between the envelope components of *M. hungatei* (the sheath, cell wall, plasma membrane, and end plugs) are seen by thin-section TEM in Fig. 1. The sheath is a single, electron-dense layer which is continuous and distinct from the cell wall and plasma membrane which serve as the outer boundaries of individual cells. The end plugs appear as alternating electron-dense and electron-translucent layers which adhere to each cell pole through their interactions with an amorphous envelope substance.

HOPG and mica substrate surfaces treated under identical conditions gave different sample distributions. HOPG proved to be an effective substrate over a range of sample concentrations, since it resulted in an even deposition of biological material. Imaging on mica surfaces was more difficult because the sample aggregated and clumped, requiring large areas of the substrate surface to be scanned before a specimen was found. For AFM, uncoated sheath appeared to be well fixed to both substrates.

Surface characterization of sheath. Examination of purified sheath by TEM of negative stains emphasized the 2.8-nm paracrystalline repeat on its outer surface and the presence of darker stained bands which denote hoop boundaries (Fig. 2). These hoop boundaries are difficult to monitor because of the moiré pattern created by imaging through two paracrystalline layers (i.e., one layer collapsed on the adjacent layer).

The identification of collapsed sheath tubes (collapsed because of the drying process of sample processing) by STM or AFM was made possible by their characteristic flattened, rectangular shape with the following dimensions: length, typically several micrometers; width, ~0.67 μm; height, 18 nm (Fig. 3). High-resolution STM images of Pt-coated sheath substantiated TEM analysis and revealed the close packing of the 2.8-nm repeats on the outer surface of the sheath and the relatively deep groves which define the hoop boundaries (Fig. 4; Fig. 2 and 4 are aligned similarly to one another for easy reference. Figure 4 is ~5× the magnification of that of Fig. 2). The 2.8-nm repeat occurred as small bumps of <1 nm in height by STM. Although distinct hoop boundaries were not observed in thin-section TEM analysis of intact cells (Fig. 1), they were apparent in thin sections of purified sheath (Fig. 4, inset) and corresponded closely with the height dimensions seen in STM.

Hoops produced from intact sheath by 2% SDS and 5% β-ME treatment (Fig. 5) retain the characteristic 2.8-nm repeat on their outer circumference by TEM negative staining (Fig. 6). STM imaging of C-coated hoops did not detect this paracrystalline repeat (Fig. 7). This was not unexpected,

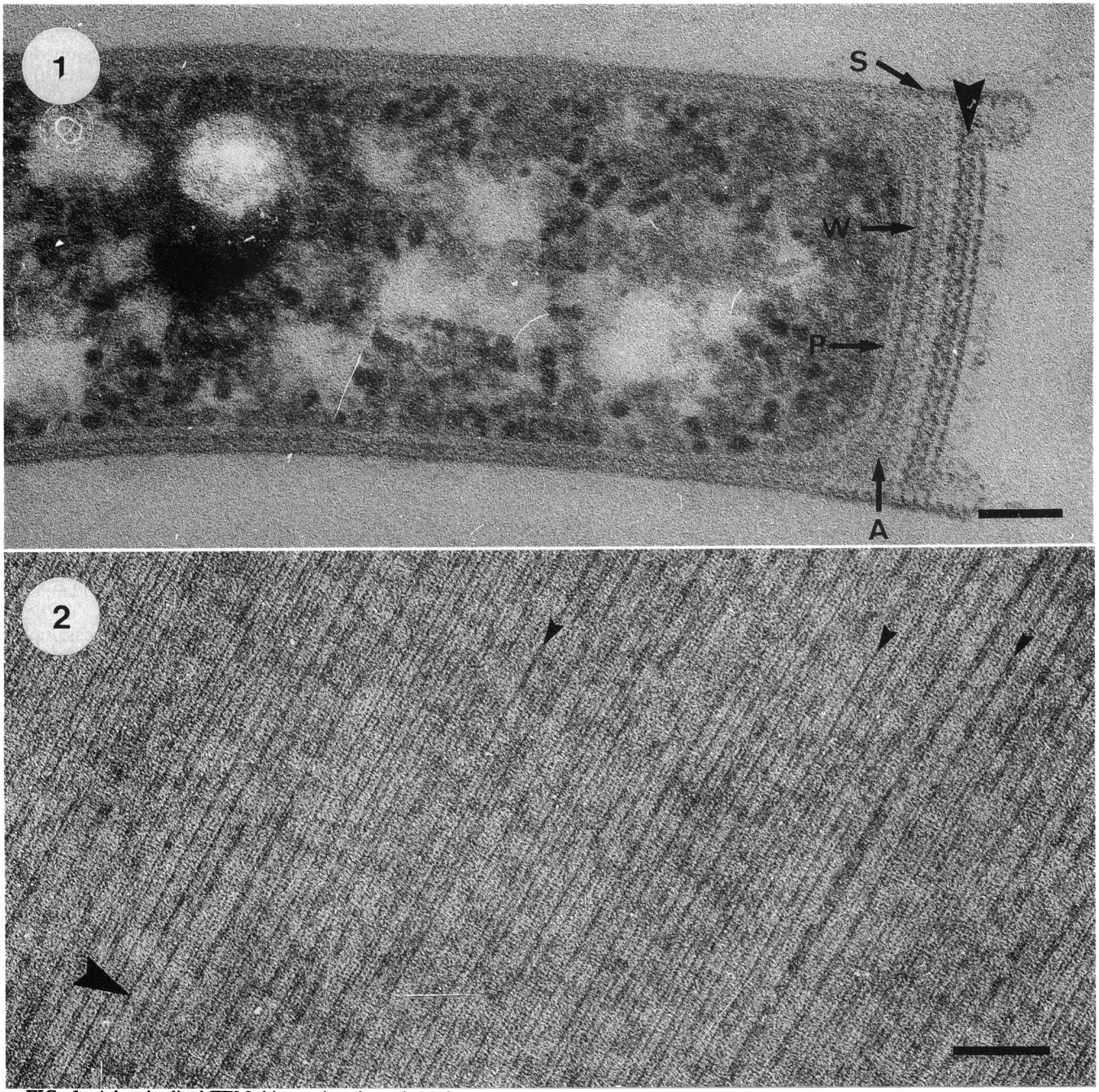

FIG. 1. A longitudinal TEM thin section through *M. hungatei*, demonstrating the relationship between the sheath (S), the cell wall (W), the plasma membrane (P) and the multilaminar end plugs (arrowhead). Amorphous material (A) is also seen. Bar, 100 nm.

FIG. 2. A TEM negative stain (2% [wt/vol] uranyl acetate) of purified sheath, demonstrating the paracrystalline nature of its surface repeat. The sheath has been aligned to correspond to the high-resolution STM image in Fig. 4. The large arrowhead corresponds to the longitudinal axis of the sheath. The dark striations (smaller arrowheads) denote hoop boundaries. Bar, 50 nm.

since STM, as a high-resolution topographical technique, has a difficult time resolving extreme vertical differences in samples. The hoop face is at ~90° to the substrate surface (Fig. 5), and the probe tip takes time to react to this extreme vertical incline; this is shown by the ~45° raster lines as the tip mounts the vertical faces of the sheath (cf. Fig. 6 and 7), yet the probe should give good resolution of the lateral surface exposed on the sheath and, since this surface is newly disclosed after β-ME treatment, its coarse texture may reflect molecular refolding due to the breakage of -S-S- bonds (31).

Surface characterization of end plugs. By thin-section TEM analysis, intact end plugs still adhered to the inside of the sheath cylinder after spheroplasting (35). In negative stains, the p6 paracrystalline structure of the entrapped end plugs was evident, and additional electron-dense material can also

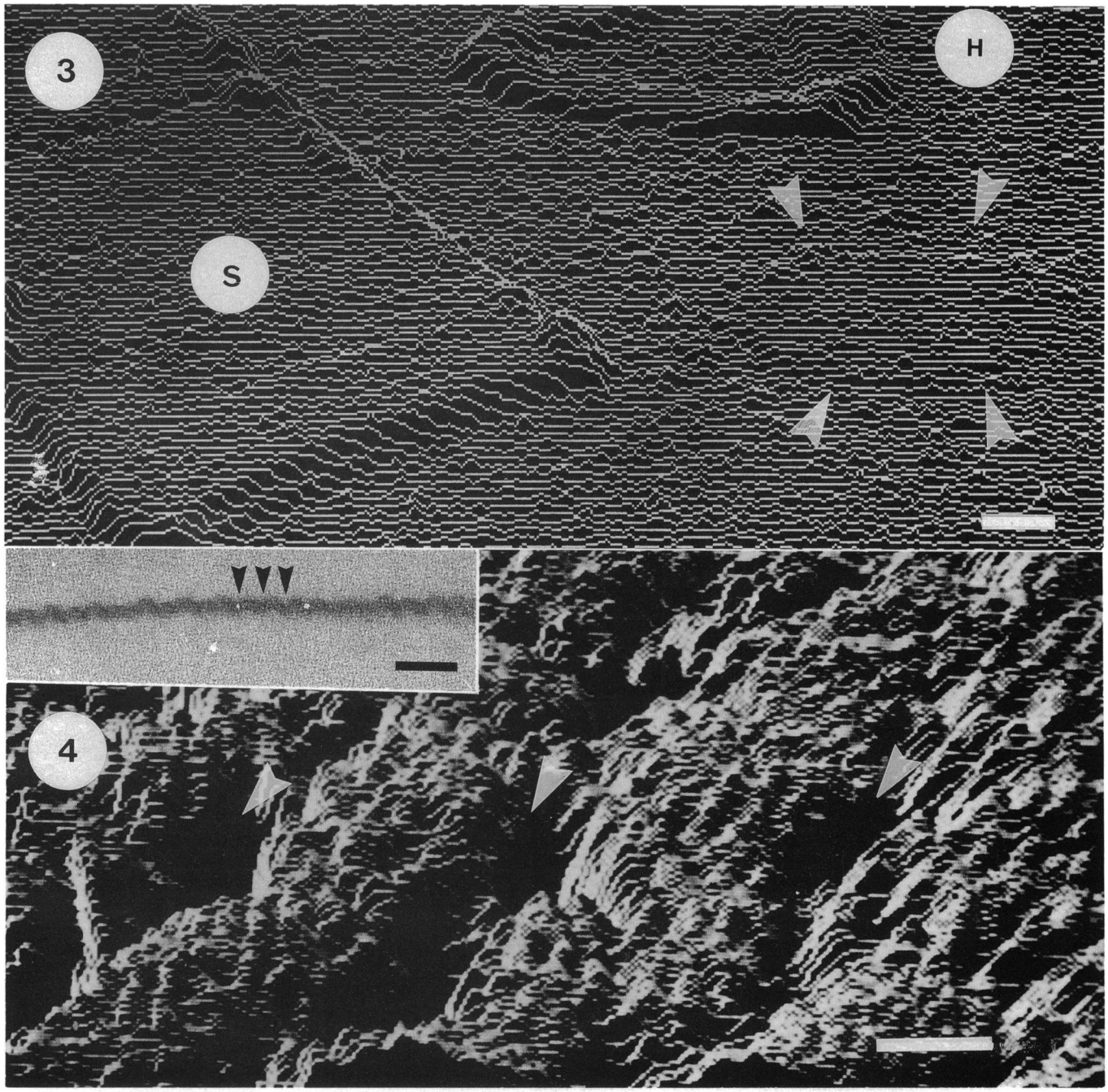

FIG. 3. A long-range STM image of a Pt-coated, collapsed sheath cylinder (S), an individual plug (white arrowheads), and several hoops stacked together (H). This demonstrates the capability of STM in discriminating, by topographical identification, the cell envelope layers of *M. hungatei*. The extreme vertical differentiation between sheath and substrate surface also serves as a convenient evaluation of STM tip quality (i.e., sharp vertical scan lines indicate a sharp tip). Bar: *x*, 100 nm; *y*, 60 nm; *z* (height), 40 nm (for the STM and AFM images, only the bar in the x orientation is provided).

FIG. 4. An STM image of Pt-coated sheath. Projections (~2.8 nm) are enhanced by setting the grey scale according to the degree of slope. The deep grooves correspond to the hoop boundaries (large arrowheads) Bar: *x*, 10 nm; *y*, 6 nm; *z*, 1.6 nm. (Inset) TEM thin section demonstrating the waveform character of the isolated sheath. The small arrowheads denote the hoop boundaries. Bar, 50 nm.

be observed on the periphery of the end plug (Fig. 8). This is a common trait of entrapped end plugs.

By using AFM, these trapped end plugs appeared as donut-shaped structures, presumably because of the additive effect of the amorphous material on the end plug periphery, and produced a ring-like structure (Fig. 9). The vertical dimensions of the entrapped end plug along with the associated amorphous ring layer were deduced from a single AFM line trace through the central portion of the donut-shaped structure (Fig. 10) by using the height of a collapsed sheath

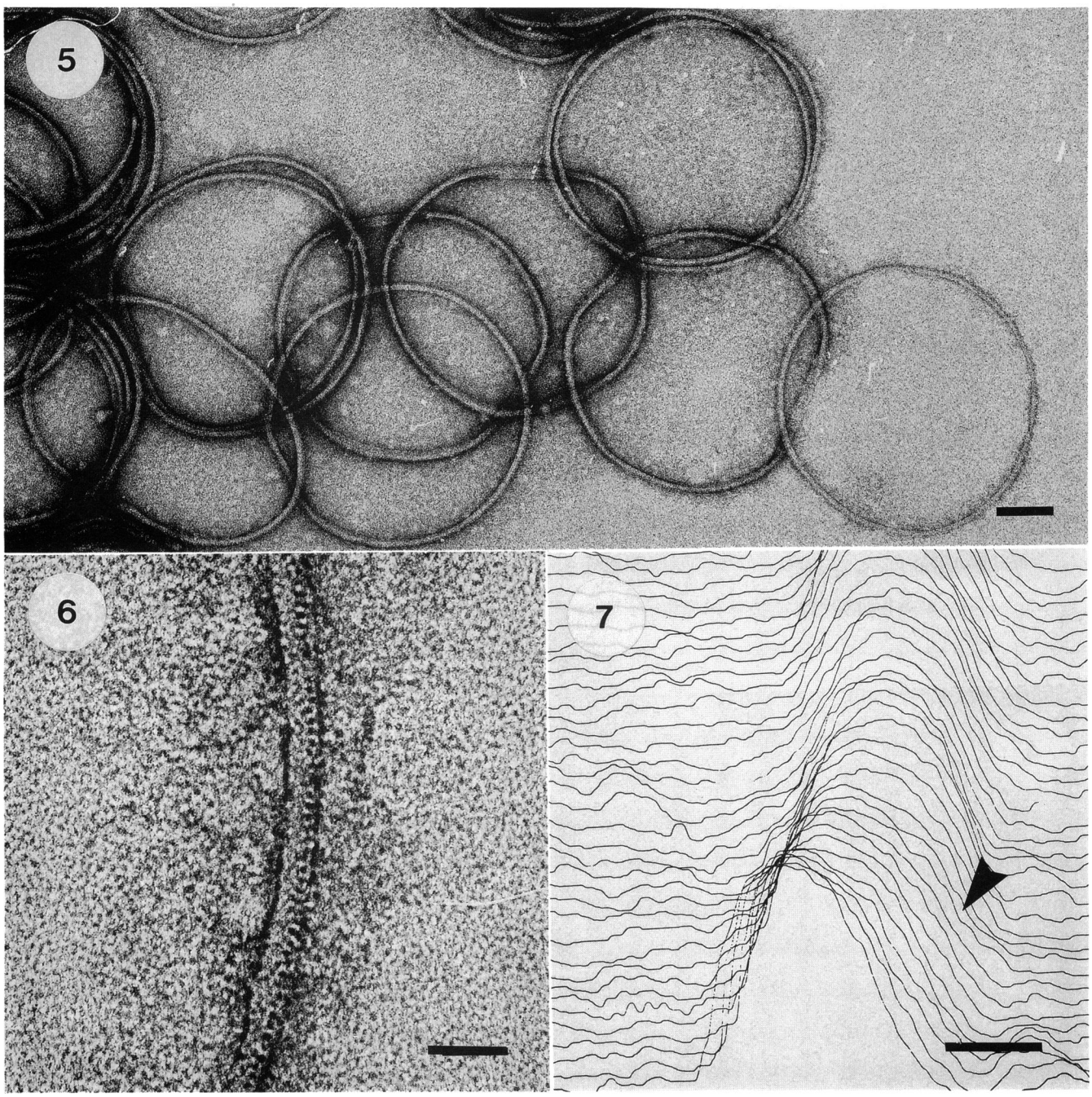

FIG. 5. A negative stain (2% [wt/vol] uranyl acetate) of hoops produced by dissolution of sheath with the SDS and β-ME treatment. Note the 2.8-nm repeat on the outer edge of these hoops. Bar, 100 nm.

FIG. 6. Higher magnification of a segment of a hoop seen in Fig. 5 which emphasizes the 2.8-nm repeat along the outer circumference of the structure. Bar, 20 nm.

FIG. 7. A STM image of a segment of a C-coated hoop. The 2.8-nm repeat on the outer edge of the hoop (arrowhead) cannot be discerned. This is not surprising, since vertical surfaces are inherently difficult to image by STM (or AFM). Bar: x, 10 nm; y, 10 nm; z, 4 nm.

cylinder (18 nm) (3) as a calibration standard. The total height of the end plug itself (minus the amorphous material, which was ~10 nm) was ~16 nm.

Under low-resolution STM imaging, end plugs were identified as coin-shaped, horizontal, flat objects having a constant circumference (Fig. 3). The height of the end plugs varied according to the number of component layers. Although intact end plugs contain multiple lamellae, these layers slip and separate from one another during their isolation (4) so that this preparation is a dispersion of unequal plug composites. It is possible that the amorphous material is the "glue" which holds the lamellae together, and its dissolution during end plug purification may be responsible for the separation. The minimum height for an exposed

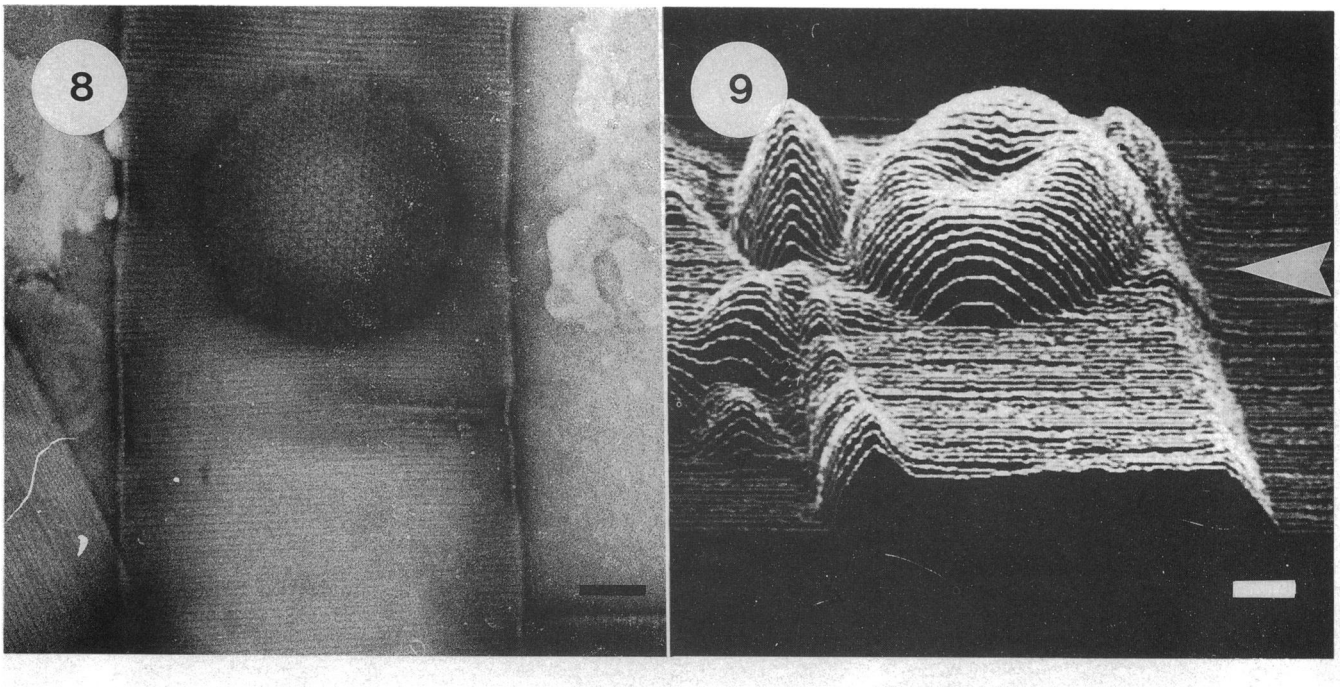

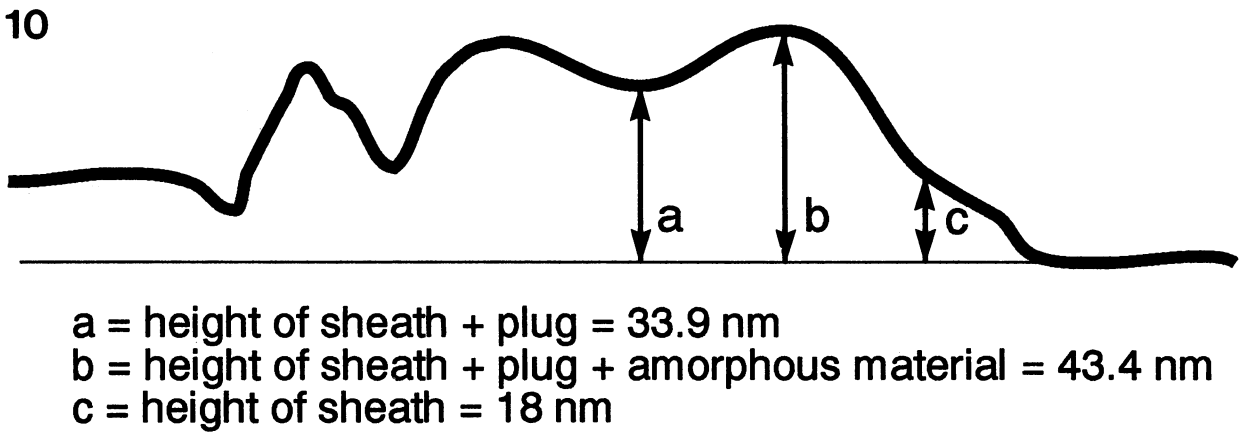

FIG. 8. A negative stain (uranyl acetate) of an end plug trapped within a collapsed sheath tube. Note the hexagonal symmetry of the multilaminar end plug. Bar, 100 nm.

FIG. 9. An AFM image of uncoated sheath containing an intact end plug (the donut-like feature). The arrow corresponds to the single-line tracing used to measure end plug dimensions in Fig. 10. Bar: *x*, 100 nm; *y*, 60 nm; and *z*, 20 nm.

FIG. 10. A single-line tracing (see arrow, Fig. 9) going across the depression in the donut structure (end plug) in the AFM image in Fig. 9. All heights were measured from the substrate surface with c as the reference point (sheath height = 18.0 nm). Accordingly, the end plug has a height of 15.9 nm (i.e., a − c), and the amorphous matrix has a height of 9.5 nm (b − a).

plug structure was ~3.5 nm, which probably corresponds to the height of a single plug layer (data not shown). Therefore, an intact end plug (~16 nm thick) presumably consists of four component plug layers.

Both Pt shadow TEM (Fig. 11) and Pt coating STM (Fig. 12) highlighted the particulate topography of the end plug, consisting of particles or hillocks arranged along threefold axes of symmetry. High-resolution STM scans of individual hillocks revealed them to be lobed and covered with numerous smaller projections (Fig. 13). The hillocks were 14 nm in diameter and 2 nm high. No detailed structure could be deciphered in the depressions surrounding each hillock, and this was presumably because of the limiting radius of the STM tip and masking of structure by the overlying Pt coating.

DISCUSSION

STM and AFM provide the technology for possible examination of biological surfaces to extremely high resolutions. We have used these instruments in conjunction with conventional TEM methodologies to study the sheath and end plugs of *M. hungatei* beyond the degree possible with STM, AFM, or TEM alone. These structures are useful biological models to use for correlation of STM, AFM, and TEM, since they are different paracrystalline planar arrays with known lattice

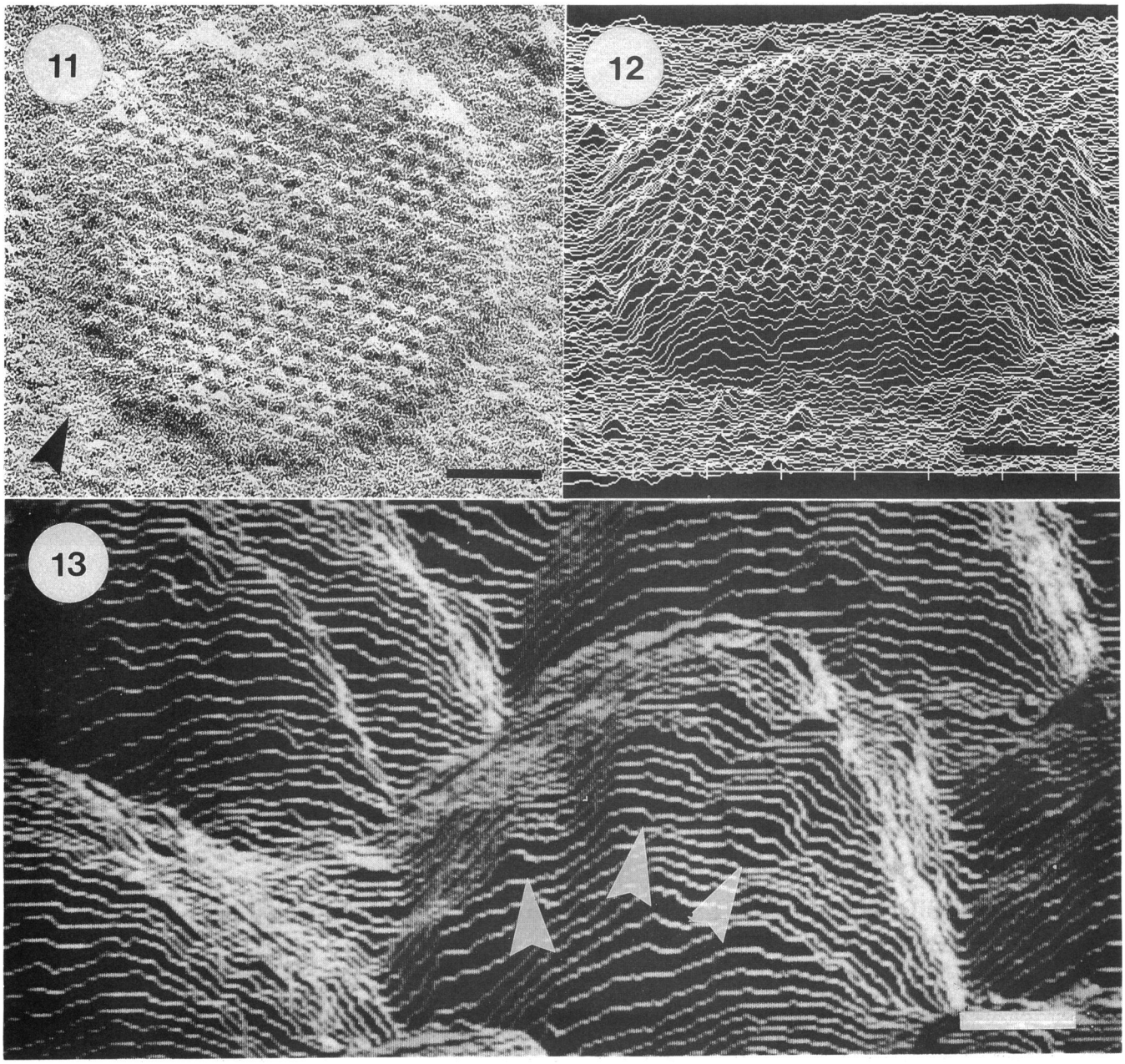

FIG. 11. A Pt-shadowed TEM image of the surface of an individual particulate end plug, demonstrating the hexagonal arrangement of the roughly circular subunits. Shadow direction is denoted by the arrow. Bar, 100 nm.

FIG. 12. An STM image of a Pt-coated end plug demonstrating the particulate nature of its surface, which corresponds to the topographical detail of the Pt-shadowed end plug examined by TEM (Fig. 11). Bar: x, 100 nm; y, 60 nm; z, 15 nm.

FIG. 13. A high-resolution STM image of the hillock structure seen on the particulate end plug surface shown in Fig. 12. Molecular detail of the individual hillock structure is evident as lobes (arrows) with numerous smaller projections. (Note: subnanometer structural information should be interpreted with caution because of grains which can be formed by the metal coating.) Bar: x, 3 nm; y, 1.75 nm; z, 0.5 nm.

parameters and are strongly bonded together so that they resist the damaging effects inherent in each of the microscopical techniques (3). Our success in resolving the surface structure of *M. hungatei* can be attributed to the integration of our STM and AFM images with our previous TEM studies on this bacterium and its components (2, 4, 5, 29–32, 34, 38).

The application of STM and AFM to biological material has to be closely scrutinized, because biological specimens are subject to a variety of tip-surface interactions that can produce artifacts. In addition to the lateral and vertical tip forces (37) which can have distorting effects on biological specimens, a number of other tip-surface interactions which produce spatial distortions have been recognized and include the following: tip shape, which acts to broaden convex structures and narrow concave structures (36); tip switching, which produces multiple images (11); tip-absorbed contaminants, which produce false images (16, 19, 36); capillary condensation of water vapor at ambient pressures, which

reduces the height measurement and possibly deforms the surface of the specimen (40); and scanning speed and feedback gain, which may result in electrical interference and structural artifacts (36). Tunneling current in particular is sensitive to the conductive properties of the surface (13, 20, 27), and consequently, STM height errors from 20 to 70% have been reported (14). To overcome imaging problems associated with poor conductivity of biological material, Guckenberger et al. (17) found that a small but sufficient conductivity from biological material can be induced at humidities of between 30 and 45%. Since it is not yet possible to distinguish these potential artifacts from specimen structure, considerable care is needed to interpret topographical detail of biological surfaces. An important control for assessing the quality of topographical detail is to utilize structural landmarks or barrier heights for the positive identification of biomacromolecules in scanned images (15, 25). Highly ordered biological surfaces (10, 16, 27, 36, 37), such as the paracrystalline proteinaceous structures examined in this study, provide mechanically rigid surfaces that contain useful landmark features for assessing image quality. From our TEM characterization of *M. hungatei* and its envelope structures, we could assess the quality of our STM and AFM images during scanning. These characteristic shapes allowed them to be readily identified at a low resolution (Fig. 3) from debris or surface defects in the substrate surface that may mimic biological surface structures.

The structural nature of the sheath is well understood because of a combination of microscopical techniques. Negative staining of pure sheath (Fig. 2) combined with optical and electron diffraction has identified its p2 unit cell (a = 2.8 nm, b = 5.6, γ = 86°) and suggest that the proteinaceous subunits have high cross β-structure (38). Pt shadowing and TEM have been used to demonstrate the wavelike character of the hoops which stack together to form the sheath (3), but the 2.8-nm paracrystalline repeat on the outer surface of the sheath (Fig. 2) was obscured. This suggests that the 2.8-nm repeat on the outer face of the sheath occurs in a relatively smooth lattice. With STM, the topography of the 2.8-nm lattice was seen for the first time across the surface of collapsed sheath tubes (Fig. 4). Although the highest resolution for the sheath came from TEM and electron diffraction studies, which detected the 0.46-nm spacing of the cross β-folding within the lattice units (38), a true appreciation for the three-dimensional orientation of the surface was only achieved by STM imaging, which highlighted the presence of grooves between the hoops. In vivo, these hoop boundaries may represent regions where the transfer of metabolites in and out of the cell could be more easily facilitated and are junctures that are more easily broken to allow filament growth and splitting (2).

We have previously examined the inner surface of the sheath by Pt shadow and TEM, which revealed the presence of ridges, separated by multiples of 2.8 nm, probably coinciding to hoop boundaries (3). In that study, STM imaging confirmed the presence of ridges on the inner surface of the sheath. However, by high-resolution hopping-mode STM, the inner surface of the sheath possessed 0.4- to 0.7-nm ridges separated by multiples of 2.8 nm on a relatively flat surface. Both techniques highlighted the same basic structures, yet Pt shadow TEM suffered from the inability to fully reconcile the three-dimensional topography of a surface (as a relatively flat zone), because the areas that are not covered by the shadowing substance (no Pt) do not provide structural information. By providing structural information over the entire surface, STM imaging has provided the highest resolution and the best topographical representation of both the inner (3) and outer (this study) surface of the sheath to date.

The inability of STM and AFM to provide accurate imaging of vertical surfaces was evident during the hoop studies. While TEM negative stains demonstrated the 2.8-nm surface repeat around the outer circumference of hoops (Fig. 6), STM imaging did not. Even at a high resolution, STM imaging did not accurately define surface details on the hoops (Fig. 7). This is likely due to the tight packing order of the 2.8-nm lattice of the outer sheath surface (determined by STM imaging [Fig. 4]) and from the inherent loss of vertical surface structure which is caused by the multiple tunneling points that can occur when scanning over a high, angular structures (height = ~15 nm; width = ~10 nm) relative to the graphite substrate. Coatings (e.g., C or Pt) also enlarge the projection of the specimen from the substrate surface (such as hoops deposited on graphite) and fill in pores or depressions, thereby reducing their size (24).

In the sheath and end plug preparation, AFM gave a remarkable appreciation of the three-dimensional orientation of the end plug and its associated amorphous components (Fig. 9) which TEM has not been able to accomplish (Fig. 8). The amorphous material could have a multiplicity of function. First, it fits around the periphery of the end plug so that only the distal end of each cell pole is tightly apposed to the end plug (Fig. 1). Second, it may somehow act as a glue to cement the lamellae of the plugs together (see results of end plug isolation, which was previously discussed). Third, it may be a region of transport of the cell envelope precursors in cell spacer development (31) and in flagellar extension (32).

To obtain these AFM images of plugs entrapped within sheath, a new physical trait of the sheath must be recognized; it must have some degree of pliability, since it collapses onto plugs and closely takes on their gross physical appearance (Fig. 9). Although pliability has been detected before in thin sections of plasmolyzed cells (31) and in STM images of individual hoops (9), the high degree of possible deformation was not appreciated. AFM has therefore provided a better qualitative understanding of the mechanical properties of sheath. The occurrence of grooves in the outer surface of the sheath (hoop boundaries [Fig. 4]) may help explain the malleable quality of the sheath by providing a flexible region for sheath bending.

The ability to break down an AFM image, line by line, allowed height measurement of both the ring of amorphous material and of the end plug, even with the sheath overlying them (Fig. 10). Since our measurements of imaged sheath height were consistent with conventional information, we expect these AFM end plug measurements to be accurate. On the basis of the minimum height determined for a single plug (~3.5 nm), the number of individual plugs must now be adjusted from three layers (4) to four layers per end plug. Such information is difficult to achieve by thin sections (TEM) through in situ end plugs (Fig. 1) because of the difficulty in unambiguously identifying single layers amongst the other associated material. Additional substance (e.g., the amorphous material) is also associated with both surfaces of these end plugs in thin section.

The structural examination of individual plugs by Pt shadow TEM and by STM of uncoated material emphasized the limitation of metal coatings on biological surfaces. Shadowing can mask minute structure (Fig. 11) and, at best, reveals only part of the structural topography present on a surface (Fig. 12). High-resolution STM was able to resolve more detail, since lobes were differentiated on each particle.

The structural examination of individual plugs by Pt shadow TEM and STM of metal-coated plugs is in broad agreement with one another (cf. Fig. 11 and 12). STM has confirmed the outermost plug layer to be of the particulate variety (4), since all intact end plugs viewed by this technique had particulate surfaces. Furthermore, STM images produced better height resolution (Fig. 12) than those previously obtained (Fig. 11). Indeed, since each plug layer possesses a relatively small finite number of regularly arranged subunits, computer image processing could achieve only limited clarification of each unit (4), i.e., the particulate layer could only be shown as circular 14-nm units connected to one another by six thin arms with the computer projection. Now, STM has added fine topographical detail to the particles, which we presume to be details of molecular folding.

ACKNOWLEDGMENTS

This study was supported by a Medical Research Council of Canada operating grant to T.J.B. The TEM was performed in the NSERC Guelph Regional STEM Facility, which has partial infrastructure support from the Natural Sciences and Engineering Research Council of Canada (NSERC). The STM and AFM are maintained by NSERC grants to B.L.B. and M.H.J.

Special thanks to C. MacKenzie for word processing.

REFERENCES

1. **Albrecht, T. R., and C. F. Quate.** 1987. Atomic resolution imaging of a nonconductor by atomic force microscopy. J. Appl. Phys. **62:**2599–2602.
2. **Beveridge, T. J., B. J. Harris, and D. G. Sprott.** 1987. Septation and filament splitting in *Methanospirillum hungatei*. Can. J. Microbiol. **33:**725–732.
3. **Beveridge, T. J., G. Southam, M. H. Jericho, and B. L. Blackford.** 1990. High-resolution topography of the S-layer sheath of the archaebacterium *Methanospirillum hungatei* provided by scanning tunneling microscopy. J. Bacteriol. **172:**6589–6595.
4. **Beveridge, T. J., G. D. Sprott, and P. Whippey.** 1991. Ultrastructure, inferred porosity, and Gram-staining character of *Methanospirillum hungatei* filament termini describe a unique cell permeability for this archaeobacterium. J. Bacteriol. **173:** 130–140.
5. **Beveridge, T. J., M. Stewart, R. J. Doyle, and G. D. Sprott.** 1985. Unusual stability of the *Methanospirillum hungatei* sheath. J. Bacteriol. **162:**728–737.
6. **Binnig, G., C. F. Quate, and C. Gerber.** 1986. Atomic force microscope. Phys. Rev. Lett. **56:**930–933.
7. **Binnig, G., H. Rohrer, C. Gerber, and E. Weibel.** 1982. Surface studies by scanning tunneling microscopy. Phys. Rev. Lett. **49:**57–60.
8. **Blackford, B. L., D. C. Dahn, and M. H. Jericho.** 1987. High stability bimorph scanning tunneling microscope. Rev. Sci. Instrum. **58:**1343–1348.
9. **Blackford, B. L., M. H. Jericho, P. J. Mulhern, C. Frame, G. Southam, and T. J. Beveridge.** 1991. Scanning tunneling microscope imaging of hoops from the cell sheath of the bacteria *Methanospirillum hungatei* and atomic force microscope imaging of complete sheathes. J. Vac. Sci. Technol. **B9:**1242–1247.
10. **Blackford, B. L., M. O. Watanabe, D. C. Dahn, M. H. Jericho, G. Southam, and T. J. Beveridge.** 1989. The imaging of a complete biological structure with the scanning tunneling microscope. Ultramicroscopy **27:**427–432.
11. **Dahn, D. C., M. O. Watanabe, B. L. Blackford, M. H. Jericho, and T. J. Beveridge.** 1988. Scanning tunneling microscopy imaging of biological structures. J. Vac. Sci. Technol. **A6:**548–552.
12. **Drake, B., C. B. Prater, A. L. Weisenhorn, S. A. C. Gould, T. R. Albrecht, C. F. Quate, D. S. Cannell, H. G. Hansma, and P. K. Hansma.** 1989. Imaging crystals, polymers, and processes in water with the atomic force microscope. Science **243:**1586–1589.
13. **Dunlap, D. D., and C. Bustamante.** 1989. Images of single-stranded nucleic acids by scanning tunnelling microscopy. Nature (London) **342:**204–206.
14. **Edstrom, R. D., X. Yang, G. Lee, and D. F. Evans.** 1990. Viewing molecules with scanning tunneling microscopy and atomic force microscopy. FASEB J. **4:**3144–3151.
15. **Fisher, K. A.** 1989. Monolayer freeze-fracture and scanning tunneling microscopy. J. Electr. Microsc. Technol. **13:**355–371.
16. **Fisher, K. A., K. C. Yanagimoto, S. L. Whitfield, R. E. Thomson, M. G. L. Gustafsson, and J. Clarke.** 1990. Scanning tunneling microscopy of planar biomembranes. Ultramicroscopy **33:**117–126.
17. **Guckenberger, R., W. Weigräbe, A. Hillebrand, T. Hartmann, Z. Wang, and W. Baumeister.** 1989. Scanning tunneling microscopy of a hydrated bacterial surface protein. Ultramicroscopy **31:**327–332.
18. **Henderson, R., and P. N. T. Unwin.** 1975. Three-dimensional model of purple membrane obtained by electron microscopy. Nature (London) **257:**28–32.
19. **Jericho, M. H., B. L. Blackford, and D. C. Dahn.** 1989. Scanning tunneling microscope imaging technique for weakly bonded surface deposits. J. Appl. Phys. **65:**5237–5239.
20. **Keller, R. W., D. D. Dunlap, C. Bustamante, D. J. Keller, R. G. Garcia, C. Gray, and M. F. Maestre.** 1990. Scanning tunneling microscopy images of metal-coated bacteriophages and uncoated, double-stranded DNA. J. Vac. Sci. Technol. **A8:**706–712.
21. **Mulhern, P. J., T. Hubbard, C. S. Arnold, B. L. Blackford, and M. H. Jericho.** 1991. A scanning force microscope with a fibre-optic-interferometer displacement sensor. Rev. Sci. Instrum. **62:**1280–1284.
22. **Patel, G. B., L. A. Roth, and G. D. Sprott.** 1979. Factors influencing filament length of *Methanospirillum hungatii*. J. Gen. Microbiol. **112:**411–415.
23. **Patel, G. B., L. A. Roth, L. van den Berg, and D. S. Clark.** 1976. Characterization of a strain of *Methanospirillum hungatii*. Can. J. Microbiol. **22:**1404–1410.
24. **Ruben, G. C.** 1989. Ultrathin (1 nm) vertically shadowed platinum-carbon replicas for imaging individual molecules in freeze-etched biological DNA and material science metal and plastic specimens. J. Electr. Microsc. Technol. **13:**335–354.
25. **Salmeron, M., T. Beebe, J. Odriozola, T. Wilson, D. F. Ogletree, and W. Siekhaus.** 1990. Imaging of biomolecules with the scanning tunneling microscope: problems and prospects. J. Vac. Sci. Technol. **A8:**635–641.
26. **Shaw, P. J., G. J. Hills, J. A. Henwood, J. E. Harris, and D. B. Archer.** 1985. Three-dimensional architecture of the cell sheath and septa of *Methanospirillum hungatei*. J. Bacteriol. **161:**750–757.
27. **Smith, D. P. E., A. Bryant, C. F. Quate, J. P. Rabe, C. Gerber, and J. D. Swalen.** 1987. Images of a lipid bilayer at molecular resolution by scanning tunneling microscopy. Proc. Natl. Acad. Sci. USA **84:**969–972.
28. **Smith, D. P. E., H. Horber, C. Gerber, and G. Binnig.** 1989. Smectic liquid crystal monolayers on graphite observed by scanning tunneling microscopy. Science **245:**43–45.
29. **Southam, G., and T. J. Beveridge.** 1991. Immunochemical analysis of the sheath of the archaeobacterium *Methanospirillum hungatei* GP1. J. Bacteriol. **173:**6213–6222.
30. **Southam, G., and T. J. Beveridge.** 1992. Characterization of a novel, phenol-soluble group of polypeptides which convey rigidity to the sheath of *Methanospirillum hungatei* strain GP1. J. Bacteriol. **174:**935–946.
31. **Southam, G., and T. J. Beveridge.** 1992. Detection of growth sites in and promoter pools for the sheath of *Methanospirillum hungatei* GP1 by use of constituent organosulfur and immunogold labeling. J. Bacteriol. **174:**6460–6470.
32. **Southam, G., M. L. Kalmokoff, K. F. Jarrell, S. F. Koval, and T. J. Beveridge.** 1990. Isolation, characterization and cellular insertion of the flagella from two strains of the archaebacterium

Methanospirillum hungatei. J. Bacteriol. **172:**3221–3228.
33. **Spong, J. K., H. A. Mizes, L. J. Lacomb, Jr., M. M. Douck, J. E. Frommer, and J. S. Foster.** 1989. Contrast mechanism for resolving organic molecules with tunnelling microscopy. Nature (London) **338:**137–139.
34. **Sprott, G. D., T. J. Beveridge, G. B. Patel, and G. Ferrante.** 1986. Sheath disassembly in *Methanospirillum hungatei* strain GP1. Can. J. Microbiol. **32:**847–854.
35. **Sprott, G. D., J. R. Colvin, and R. C. McKellar.** 1979. Spheroplasts of *Methanospirillum hungatii* formed upon treatment with dithiothreitol. Can. J. Microbiol. **25:**730–738.
36. **Stemmer, A., and A. Engel.** 1990. Imaging biological macromolecules by STM: quantitative interpretation of topographs. Ultramicroscopy **34:**129–140.
37. **Stemmer, A., A. Hefti, U. Aebi, and A. L. Engel.** 1989. Scanning tunneling and transmission electron microscopy on identical areas of biological specimens. Ultramicroscopy **30:**263–280.
38. **Stewart, M., T. J. Beveridge, and G. D. Sprott.** 1985. Crystalline order to high resolution in the sheath of *Methanospirillum hungatei*: a cross-beta structure. J. Mol. Biol. **183:**509–515.
39. **Travaglini, G., H. Rohrer, M. Amrein, and H. Gross.** 1987. Scanning tunneling microscopy on biological matter. Surf. Sci. **181:**380–390.
40. **Weisenhorn, A. L., P. K. Hansma, T. R. Albrecht, and C. F. Quate.** 1989. Forces in atomic force microscopy in air and water. Appl. Phys. Lett. **54:**2651–2653.
41. **Wickramasinghe, H. K.** 1990. Scanning probe microscopy: current status and future trends. J. Vac. Sci. Technol. **A8:**363–368.
42. **Zeikus, J. G., and V. G. Bowen.** 1975. Fine structure of *Methanospirillum hungatii*. J. Bacteriol. **121:**373–380.